




Microstructure evolution, dielectric response, and conduction mechanism of $\text{La}_{1-x}\text{Y}_x\text{FeO}_3$, ($0 < x < 0.3$) annealed perovskites synthesized via a sol–gel combustion technique

Ahmed H. Ibrahim^{1,*} , S. Mosaad¹, and E. Elesh²

¹ Materials Science Laboratory, Department of Physics, Faculty of Science, Suez Canal University, Ismailia 41511, Egypt

² Department of Physics, Faculty of Science, Port Said University, Port Said 41522, Egypt

Received: 24 October 2023

Accepted: 31 January 2024

Published online:
24 February 2024

© The Author(s), 2024

ABSTRACT

The structural and dielectric characteristics of nano-crystalline $\text{La}_{1-x}\text{Y}_x\text{FeO}_3$, ($0 < x < 0.3$) perovskite samples synthesized through the citrate auto-combustion route were investigated. The findings of X-ray diffraction (XRD) analysis revealed that the synthesized perovskites exhibited a polycrystalline orthorhombic structure with a space group $Pnma$. Furthermore, the tolerance factor was indicative of the phase stability of the orthoferrite series. Based on the refined XRD data, the size of the crystallites was estimated to be between 11.9 and 18.5 nm using size-strain plots (SSP). To gain more insight into the crystal structure, high-resolution transmission electron microscopy (HRTEM) was employed. The estimated size based on HRTEM calculations agreed with the XRD findings. The influence of annealing temperature on the frequency dependence of the dielectric response was thoroughly investigated for nano-crystalline $\text{La}_{1-x}\text{Y}_x\text{FeO}_3$ perovskites. The investigation took place at room temperature as well as different annealing temperatures, with a comprehensive frequency range of 50 Hz to ~ 2 MHz. The incorporation of Y^{3+} ions into LaFeO_3 (LFO) has resulted in a significant enhancement of the dielectric constant values. This improvement is attributed to the successful integration of Y^{3+} ions, which have effectively modified the electrical properties of LFO. Furthermore, the annealing has been shown to enhance both the values of the dielectric constant, $\epsilon_1(\omega)$ and $\epsilon_2(\omega)$, which are critical parameters for electronic devices. Based on a power law response, the AC conductivity displays an increase with dopant concentration and frequency. Additionally, it has been noted that the activation energy value for LFOY30 is slightly reduced by 0.01 eV in comparison to pure LFO. The AC conductivity of LFOY30 was observed to increase with thermal annealing over the temperature range of 333 K to 463 K. This result confirms the occurrence of thermally activated conduction in the material. Based

Address correspondence to E-mail: ahmed_abdel-hamid@science.suez.edu.eg

E-mail Addresses: sara_mosaad@science.suez.edu.eg; eman_phs@yahoo.com

on this finding, LFOY30 is deemed appropriate for use in applications that require effective heat dissipation. The frequency exponent, s , decreases with increasing temperature from 0.87 to 0.56 for LFO and from 0.488 to 0.42 for LFOY30, respectively, which is associated with the correlated barrier hopping (CBH) model. The maximum barrier height (W_M) was around 0.26 eV. The loss tangent ($\tan\delta$) variation was estimated as a function of frequency at different dopant concentrations and temperatures. Doping and annealing have been identified as appropriate measures for enhancing the electrical properties of the $\text{La}_{1-x}\text{Y}_x\text{FeO}_3$ system, thereby making it a useful material for electronic devices.

1 Introduction

Perovskite-type materials have become a promising study area for researchers owing to their robust structure and a diverse range of advantageous properties, including stability, dielectric behavior, optical response, magnetic behavior, piezoelectricity, and catalytic activity [1–3]. Perovskite-type ceramics with the general formula ABO_3 are a class of ceramics composed of cations A and B derived from lanthanides and alkali earth metals, respectively, while O represents oxygen ions [1–3]. Furthermore, the potential applications of these materials are extensive, spanning across a diverse range of devices. These devices include memories, tunable microwave displays, fuel cells, gas sensors, oxygen-permeable membranes, actuators, ultrasonic motors, sensors, and capacitors [4–7]. The room temperature behavior of LaFeO_3 (LFO) is characterized by ferroelasticity [8]. This is attributed to a spontaneous lattice strain of $\sim 2.4 \times 10^{-4}$ [8] arising from atomic displacements of La, O1, and O2 in the individual with invariant Fe at the inversion center. This effect confers additional functionality to LFO and augments its multi-ferroic properties. Moreover, doped LFO is an exceptional material for various applications due to its high room temperature dielectric constant (~ 500 – 800), low loss, and superior commitment toward spontaneous polarization and magnetization. With these remarkable properties, it finds tremendous use as an ethanol sensor, a hot electrode for MHD power generation, and in solid oxide fuel cells (SOFCs) [9, 10]. Furthermore, the unique optoelectronic properties and narrow band gap of LFO have been found to confer visible light photocatalytic activity. This discovery, as reported in [3], underscores the potential of LFO as a promising candidate for various applications in the field of catalysis. For the aforementioned reasons, the doped Lanthanum orthoferrite is undoubtedly a superior multifunctional material

when compared to other ceramic materials. At ambient temperatures, the RFeO_3 polycrystalline material presents a distorted perovskite structure characterized by a space group of pnma or Pbnm [11]. Achieving a uniform size distribution of nanoparticles in perovskites is critical in enhancing their characteristics. To this end, significant attention is paid to the controlled synthesis of RFeO_3 nanomaterials. By carefully regulating the synthesis process, a consistent and homogeneous distribution of nanoparticles can be achieved, enhancing the desirable properties of perovskites. This emphasis on controlling the synthesis of RFeO_3 nanomaterials reflects the importance of precision and attention to detail in manufacturing high-quality perovskite materials. Perovskite-type nanomaterials exhibit unique structural, electrical, and dielectric properties. It is possible to modify these properties by carefully selecting rare-earth elements at the tetrahedral site and transition metal ions at the octahedral site. By doing so, the characteristics of the nanomaterials can be tailored to meet specific requirements for various applications. This approach is particularly useful for designing new materials with enhanced functionality and performance. Therefore, it is imperative to explore the potential of perovskite-type nanomaterials for various technological and scientific fields [12]. Additionally, the observation of replacement on the A and/or B sites has enhanced the electrical characteristics. Several other forms of substitution have been investigated in previous studies. For instance, examples include $\text{La}_{0.33}\text{Sr}_{0.66}\text{FeO}_3$ [13], $\text{La}_{1-x}\text{Zn}_x\text{FeO}_3$ [14], $\text{La}_{0.5}\text{Al}_{0.5}\text{FeO}_3$ [15], and $\text{La}_{1-x}\text{Ca}_x\text{FeO}_3$ [16]. The Perovskite-type ceramics demonstrate the intriguing characteristics of electrical materials, including but not limited to a high dielectric constant, low dielectric loss, high electrical conductivity, thermal stability, ferroelectricity, and piezoelectricity. Hence, incorporating divalent or trivalent ions into the La or Fe sub-lattices has been investigated to enhance these

features [13–18]. Orthoferrites may be synthesized by a variety of techniques, including the solid-state approach [17], combustion method [18], hydrothermal method [19], electron spin route [20], and coprecipitation method [21]. Nonetheless, developing a straightforward, cost-effective, and environmentally friendly synthesis method for the perovskite material LaFeO_3 , which possesses several useful characteristics, remains a significant issue. In this study, we employed the sol–gel auto-combustion technique to fabricate nanostructured $\text{La}_{1-x}\text{Y}_x\text{FeO}_3$ materials ($x = 0.00, 0.05, 0.1, 0.15, 0.25, \text{ and } 0.30$). This approach has several advantages, including improved precursor mixing, reduced energy usage, lower temperature requirements, and consistent homogeneity in the resulting product [22]. *D. Triyono et al.* [23] reported the synthesis of $\text{e La}_{1-x}\text{Sr}_x\text{FeO}_3$ ($x = 0.1, 0.2, 0.3, \text{ and } 0.4$) via a citrate auto-combustion approach and investigated their structure and dielectric properties. They employed Impedance spectroscopic experiments to elucidate the electrical characteristics in relation to the frequency range (100 Hz to 1 MHz) under different temperatures (300–373 K). They clarified the presence of tiny polarons as charge carriers within the grain and grain border through their electrical conductivity studies. The inclusion of Sr-substitution increased both the dielectric constant and electronic conductivity. The greatest values were seen in $\text{La}_{1-x}\text{Sr}_x\text{FeO}_3$, specifically at $x = 0.4$. *L. John Berchmans et al.* [24] also discovered that the electrical conductivity of the synthetic LaFeO_3 compounds substituted with Sb increases with rising measurement temperature. They revealed that when frequency increases, the dielectric constant decreases. The observed behavior of the synthesized materials indicates semiconducting characteristics, as evidenced by the temperature-dependent direct current (d.c.) conductivity. Further, the study conducted by *A. Tiwari et al.* [25] examined the impact of Barium doping at the A-site and nickel doping at the B-site in the synthesis of LaFeO_3 (LFO) ceramics using the Coprecipitation route. The researchers discovered that using Barium as a dopant leads to an enhanced dielectric nature, which can be attributed to the increased polarizability shown by the Ba ions. The ionic conductivity of LFO exhibits higher values when doped with Ni compared to its doping with Ba. This can be attributed to the phenomenon of toggling, where the ionic state of Fe^{3+} is altered to Fe^{4+} to maintain charge balance. They found that the incorporation of barium into LFO leads to an enhancement in its capacitive

properties, which is directly proportional to the concentration of Ba. In their study, *M. Asif et al.* [26] performed an investigation on the dielectric behavior of $\text{Y}_{1-x}\text{Pr}_x\text{FeO}_3$ ($0 \leq x \leq 0.16$) ceramics at ambient temperature. The study encompassed a wide frequency range from 1 MHz to 3 GHz. They found that adding Pr considerably increased the dielectric constant. A peak shift toward higher frequencies was observed, which may be ascribed to the increase in dopant concentration, a phenomenon believed to be controlled by the Maxwell–Wagner–Sillars polarization mechanism.

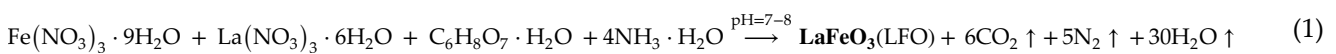
The current study is focused on examining various aspects of structural, microstructural, AC conductivity, and dielectric characteristics of high-quality $\text{La}_{1-x}\text{Y}_x\text{FeO}_3$ ceramics ($x = 0.00, 0.05, 0.10, 0.15, 0.25, \text{ and } 0.30$) produced by citrate–nitrate auto-combustion route. The conductive mechanism and the dielectric properties are investigated. To the best of our knowledge, a full investigation of Y co-substitution in $\text{La}_{1-x}\text{Y}_x\text{FeO}_3$ has not been undertaken. An extensive literature analysis revealed that annealing significantly changes the material's structural, optical, electrical, and dielectric behavior, reflected in many electronic applications such as sensors, energy storage systems, and electronic devices. Consequently, an investigation was conducted to evaluate the influence of thermal annealing on the dielectric properties and electrical conductivity of perovskite-type ceramics. Subsequently, a comprehensive discussion ensued.

2 Experimental details

2.1 Materials and methods

Analytical quality of $\text{Fe}(\text{NO}_3)_3 \cdot 9\text{H}_2\text{O}$, $\text{La}(\text{NO}_3)_3 \cdot 6\text{H}_2\text{O}$, and citric acid monohydrate ($\text{C}_6\text{H}_8\text{O}_7 \cdot \text{H}_2\text{O}$) were used as raw materials to synthesize high-quality nanostructured $\text{La}_{1-x}\text{Y}_x\text{FeO}_3$, with ($x = 0.00, 0.05, 0.10, 0.15, 0.25, \text{ and } 0.30$). All chemicals were purchased from Sigma-Aldrich with a minimum purity of 99.9%, and no extra purification was required. The chemicals were combined in stoichiometric proportions within a 500-ml glass beaker and subjected to heating at a temperature of 70–80 °C on a hot plate for approximately 20 min. The mixture was subjected to rigorous stirring at 1350 revolutions per minute throughout the experimental process, employing a magnetic stirrer to ensure homogeneity. The molar ratio of metal nitrates to citric acid (fuel) was intentionally kept at a constant ratio

of 1:1. In order to achieve a pH of 7–8 and establish stability in the nitrate-citrate solution, a small quantity of 33.3% aqueous ammonia solution was added dropwise. During this process, the solution was maintained at a temperature range of 70–80 °C while continuously stirred. The as-prepared ceramics were acquired by decomposing the dried gel in an open environment at a temperature range of 190–200 °C. Upon ignition in the air, a dry gel underwent thermochemical combustion, ultimately transforming into a deep brown as-prepared powder. The increase in Y^{3+} concentration resulted in a corresponding increase in the darkness of the powder. The thermochemical reaction for this synthesis is given in Eq. (1).



2.2 Characterization techniques

A small quantity of the initially prepared powder was used to determine its phase purity, structure, and crystallite parameters (size and lattice strain) using an X-ray powder diffractometer (X'Pert pro PANalytical MRD equipment) with Cu-K α radiation ($\lambda = 1.54056 \text{ \AA}$). The lattice parameters of each composition were determined precisely by implementing the Rietveld approach [27–29]. The X-ray diffraction (XRD) patterns underwent thorough Rietveld refinement analysis using the FullProf software. The refinement procedures for the studied orthoferrites were initiated by utilizing the crystallographic data of LaFeO₃ [30]. Subsequently, the patterns underwent structural refinement at a counting rate of 2° (2 θ) per minute per step. This process ensured that the orthoferrites were accurately analyzed and their structural properties were optimally refined. This method refined the lattice parameters, atomic coordinates, thermal parameters, occupancies, and microstructural parameters, specifically the average crystallite size and non-uniform lattice strain, for all these synthesized compositions. An asymmetric pseudo-Voigt function was employed in the structural analysis to delineate the peak shapes across diverse samples. The estimation and visualization of electron density within the unit cell have been conducted by utilizing the GFourier tool, which is a part of the FullProf package. The procedure has been executed precisely and accurately to obtain the most conclusive and reliable results. A comprehensive exposition of the mathematical methodologies

employed in the Rietveld analysis is available in many literatures [31–38]. The morphology and size of the samples were estimated by utilizing a tiny quantity of powder evenly suspended in alcohol with a purity of 99.99% and, after that, subjected to sonication for 15 min. This solution was applied onto a Carbon-coated copper grid and utilized for high-resolution transmission electron microscopy (HRTEM) analysis. The HRTEM analysis was conducted utilizing a JEOL-JEM 2100 instrument, operated at an acceleration voltage of 200 kV. The perovskite-type ceramics La_{1-x}Y_xFeO₃ (where 0 < x < 0.3) were subjected to a high-pressure treatment of approximately 450 MPa using a hydraulic press. The resulting product was a

cylindrical pellet of optimal dimensions, measuring 1.2 cm in diameter and 0.09 cm in thickness. The pellets are sandwiched between two gold electrodes to act as ohmic contacts. The dielectric characteristics of La_{1-x}Y_xFeO₃ (0 < x < 0.3) pellets were determined using an LCR bridge (Hioki 3532 Hitester with a frequency range of 50 Hz–2 MHz). Temperature-dependent measurements were performed on La_{1-x}Y_xFeO₃ at x = 0 and 0.3 from 293 to 473 K.

3 Results and discussion

3.1 Structural characteristics

The XRD patterns of La_{1-x}Y_xFeO₃, (x = 0.00, 0.05, 0.10, 0.15, 0.25, and 0.30) are depicted in Fig. 1. The observed disappearance of reactant peaks and the emergence of the corresponding perovskite peaks provide conclusive evidence of the formation and completion of the reaction. These data affirm the successful synthesis of the La_{1-x}Y_xFeO₃ perovskites under investigation, providing valuable insight into their physical and chemical characteristics. The diffraction patterns were investigated using the Rietveld method, resulting in the identification of peaks corresponding to the (101), (121), (220), (202), (240), (242), and (204) planes. These peaks agreed with the (JCPDS: No. 88-0641) database. It was observed that a negative x/a site coordinate value indicates a transition from the symmetric development of Pnma to Pbnm [39]. According to the XRD data and Rietveld analysis,

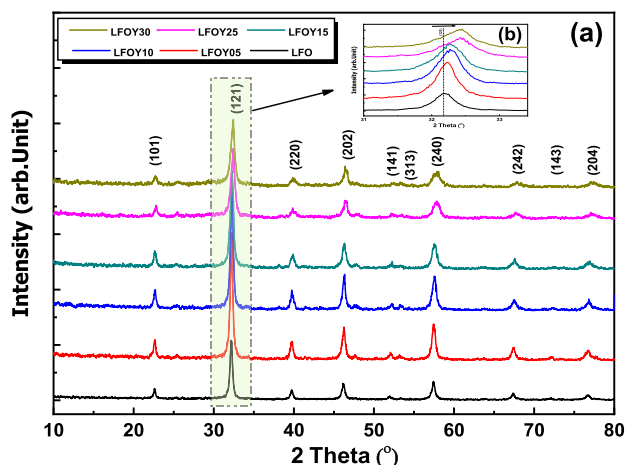


Fig. 1 **a** XRD patterns of the as-prepared perovskite system $\text{La}_{1-x}\text{Y}_x\text{FeO}_3$, ($x=0.00, 0.05, 0.10, 0.15, 0.25,$ and 0.30) perovskites, **b** Enlarged view of XRD patterns of the orthorhombic perovskite materials at (121) plane

no secondary phases have been developed, as demonstrated in Fig. 3a–f. Additionally, it demonstrates the monophasic formation of the perovskite compositions within the XRD detection range. The smaller ionic radius of the Y^{3+} (1.019 Å) relative to the La^{3+} (1.16 Å), as reported by *Y.M. Abbas et al.* [40], causes a shift toward larger 2θ values when the Y^{3+} is increased in the host La^{3+} crystal structure, as shown in Fig. 1. The tolerance factor suggested by Goldschmidt [40] serves as a metric for assessing the stability and deformation of a perovskite crystal structure. The ratio of ionic radii determines the Goldschmidt tolerance factor (t) for $\text{La}_{1-x}\text{Y}_x\text{FeO}_3$ perovskites and might be expressed as follows:

$$t = \frac{(1-x)R_{\text{La}^{3+}} + xR_{\text{Y}^{3+}} + R_{\text{O}^{2-}}}{\sqrt{2}(R_{\text{O}^{2-}} + R_{\text{Fe}^{3+}})}, \quad (2)$$

where $R_{\text{La}^{3+}}$, $R_{\text{Y}^{3+}}$, $R_{\text{O}^{2-}}$, and $R_{\text{Fe}^{3+}}$ are the ionic radii of the La, Y, O, and Fe ions, respectively. Goldschmidt tolerance factors (t) are calculated using Eq. (2). A few A-site cation size suggests that Goldschmidt’s tolerance factor will be observed, which will be less than 1. Consequently, the octahedra represented by $[\text{BO}_6]$ will undergo tilting to achieve maximum space filling. The study by *Y.M. Abbas et al.* reported that the perovskite exhibits structural stability in the range of 0.75 to 1.0. Moreover, the material assumes a cubic configuration when t exceeds 0.95. [40]. This stability is maintained in the case of an ideal cubic structure,

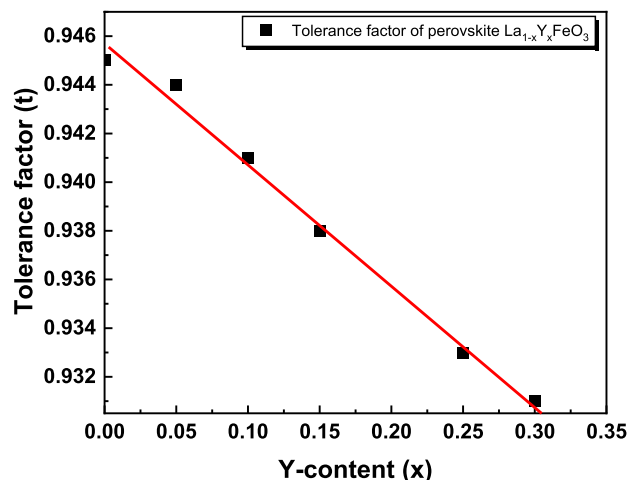


Fig. 2 The variation of the tolerance factor with Y-content (x)

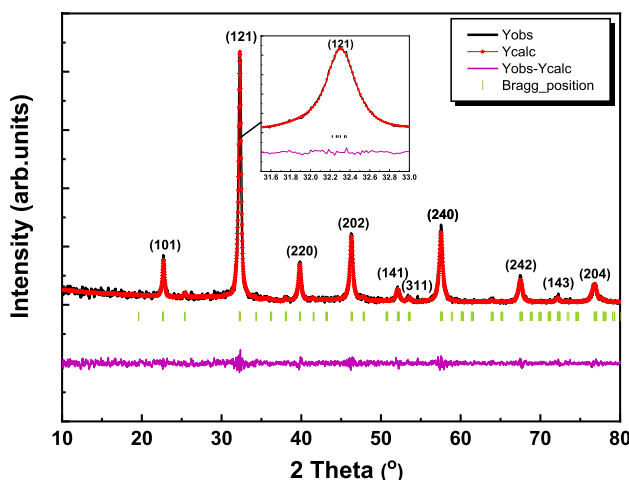


Fig. 3 Rietveld refinement profile of XRD of the as-prepared LaFeO_3 (LFO). The black line represents the observed patterns, the red points represent the calculated patterns, the green vertical line represents the position of Bragg reflections, and the violet line represents the difference between observed and calculated intensities

where t equals 1 For an ideal cubic structure ($t = 1$), for stabilizing the perovskite structure, t must be between 0.75 and 1.0 and cubic when ($t > 0.95$) [40, 41]. The orthorhombic symmetry of the perovskites is confirmed by (t) values in the range of ($0.85 > t > 0.95$) [40]. The ionic radii of La^{3+} and Y^{3+} are 1.216 Å and 1.075 Å, respectively, when subjected to ninefold coordination. Conversely, Fe^{3+} and O^{2-} possess ionic radius of 0.55 Å and 1.42 Å, respectively, under six fold coordination. The synthesized perovskites display

an orthorhombic structure, which has been authenticated by tolerance factor values that fall within the range of 0.85 to 0.95, as demonstrated in Fig. 2. The observed trend in the t values indicated a decrease as the concentration of Y^{3+} increased, which can be attributed to the displacement of La^{3+} caused by the variation in their respective ionic radii. The tolerance factor's correlation with increasing concentrations of Y is depicted in Fig. 2, affirming the compositions' stable orthorhombic structure. The distortion observed in the $\langle FeO_6 \rangle$ octahedron may be attributed to the larger size of the $R_{Fe^{3+}}$ cation, leading to the octahedron's tilt. This tilting, in turn, caused a shift in the Fe–O–Fe geometry. The synthesized ceramics exhibited monophasic characteristics and, as evidenced by the well-fitted refinement patterns for ($x = 0.00, 0.05, 0.10, 0.15, 0.25,$ and 0.30), can be attributed to the SG Pnma. Figure 3 displays the Rietveld refinements profile of the XRD patterns of $LaFeO_3$. The Rietveld profile fitting of the other ceramics $La_{1-x}Y_xFeO_3$ ($x = 0.05, 0.10, 0.15, 0.25,$ and 0.30) is presented in Fig. S1a–e (Supplementary materials). The data presented in Table S1 reveal that the structural and fitting parameters were accurately determined, thus ensuring high-quality fittings. The goodness of fit parameter, represented by χ^2 , was less than 2, indicating a highly accurate fitting of the experimental diffraction profile as illustrated in Fig. 3 and Table S1. The present work compares the six orthorhombic orthoferrites, revealing that the addition of the Y results in a significant decrease in unit cell volume, as shown in Fig. 4. This result can be attributed to

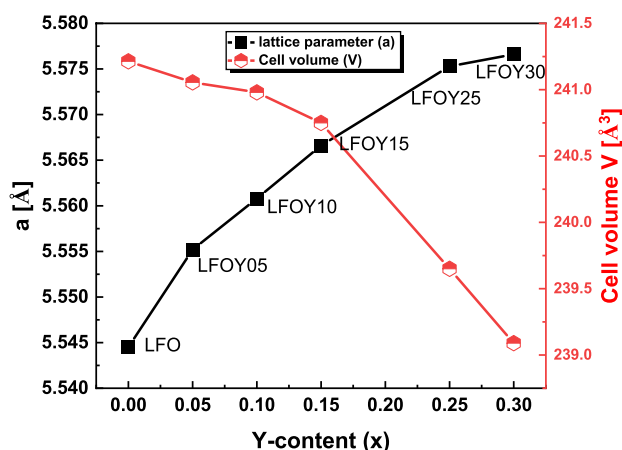


Fig. 4 The correlation between Y-content (x) and the lattice parameter (a), as well as the cell volume (V) in the perovskite system $La_{1-x}Y_xFeO_3$

the relatively smaller ionic radius of Y^{3+} in comparison to La^{3+} . Some of the Fe^{3+} ions can be converted to Fe^{4+} and Fe^{5+} (which have lower ionic radii), decreasing the unit cell. This phenomenon, known as lattice reduction, exhibits anisotropy, where the lattice parameters b and c experience a minor reduction, while the lattice parameter (a) shows a minor increase. This observation suggests that an increase in yttrium concentrations leads to a significant distortion in the lattice geometry. These observations are depicted in Fig. 4. The effect of the Y substitution on the lattice strain in the structure has been determined by means of a size-strain equation [42]. It is worth noting that the crystallite size and the lattice microstrain are interrelated, and this relationship is described by Eq. (3).

$$(d_{hkl}\beta_{hkl}\cos\theta)^2 = \frac{K}{D}(d_{hkl}^2\beta_{hkl}\cos\theta) + \left(\frac{\varepsilon}{2}\right)^2, \quad (3)$$

where d_{hkl} is the interplanar spacing, k is the shape constant (0.9), β_{hkl} is the full width at half maximum (FWHM) for each hkl plane, D is the average crystallite size, and ε is the lattice strain. Figure 5 shows the plots of $(d_{hkl}\beta_{hkl}\cos\theta)^2$ vs. $d_{hkl}^2\beta_{hkl}\cos\theta$ for the fitted XRD patterns of LFO, and the size-strain plots for the other perovskite compositions are illustrated in Fig. S2a–e (Supplementary materials). The slopes and intercepts were calculated using linear fitting of the experimental data points. The mean crystalline size values were acquired directly from the slope values, while the lattice strain values were produced by calculating the square root of the intercepts. Table S1 presents the

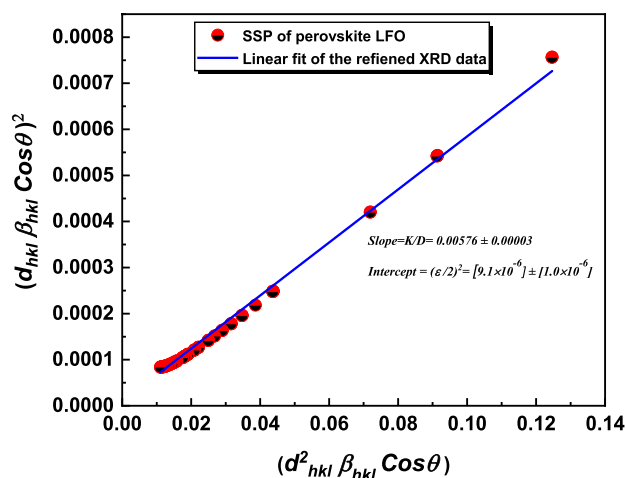


Fig. 5 The crystallite size and lattice strain calculation using size-strain plots (SSP) for LFO

mean crystallite size and lattice strain values of the compositions, which are determined through a size-strain plot (SSP). The synthesized perovskites exhibit estimated crystallite sizes ranging from 11.9 ± 0.01 nm to 18.5 ± 0.02 nm, along with non-uniform microstrains that vary from 4.0×10^{-3} for LFOY05 to 8.5×10^{-3} for LFOY15.

The use of GFourier software in Rietveld refinement is a notable outcome that facilitates the visualization and characterization of electron density within the unit cell. The graphical representation of crystals plays a crucial role in identifying the atomic positions of constituent elements throughout the unit cell. This information is essential for understanding the properties and behavior of crystals. One can determine the location of a larger element in the unit cell by analyzing the thickness of the electron density contours relative to other elements. The calculation of the scattering density $\rho(x, y, z)$ using the fast Fourier transform (FFT) formula is conventionally utilized for this purpose [39, 40].

$$\rho(x, y, z) = \frac{1}{V} \sum_{hkl} |F_{(hkl)}| e^{\{-2\pi i(hx+ky+lz-\alpha_{hkl})\}} \quad (4)$$

The magnitude of the structure factor is represented by $F(hkl)$, while the phase angle of each Bragg reflection is denoted by α_{hkl} . Figure 6 shows the 3-D electron density representation of the selected LFO and LFOY25. The figure displays the zero-level density contour in black, while the regions colored in red to violet-brown signify a progressive rise in electron density levels surrounding the La cation. Significant deviations in the oxygen positions within the unit cell are observed compared to the Fe and La | Y positions. The 4c Wyckoff positions exhibit robust positive peaks. The investigated perovskite system comprises Fe and La cations positioned at $(0, 0, 0.5)$ and $(0.028, 0.25, 0.993)$, respectively. Figure 6a, b demonstrates a significant contrast in the scattering density across the O, La | Y and Fe ions.

3.2 Microstructural analysis

HRTEM micrographs were used to examine the microstructure of the perovskite $\text{La}_{1-x}\text{Y}_x\text{FeO}_3$ nanocrystallites ($x = 0.00, 0.05, 0.10, 0.15, 0.25, \text{ and } 0.30$). The HRTEM images of the LFYO nanoparticles (NPs) in the orthoferrite system are shown in Fig. 7a–d. The composition of the particles was

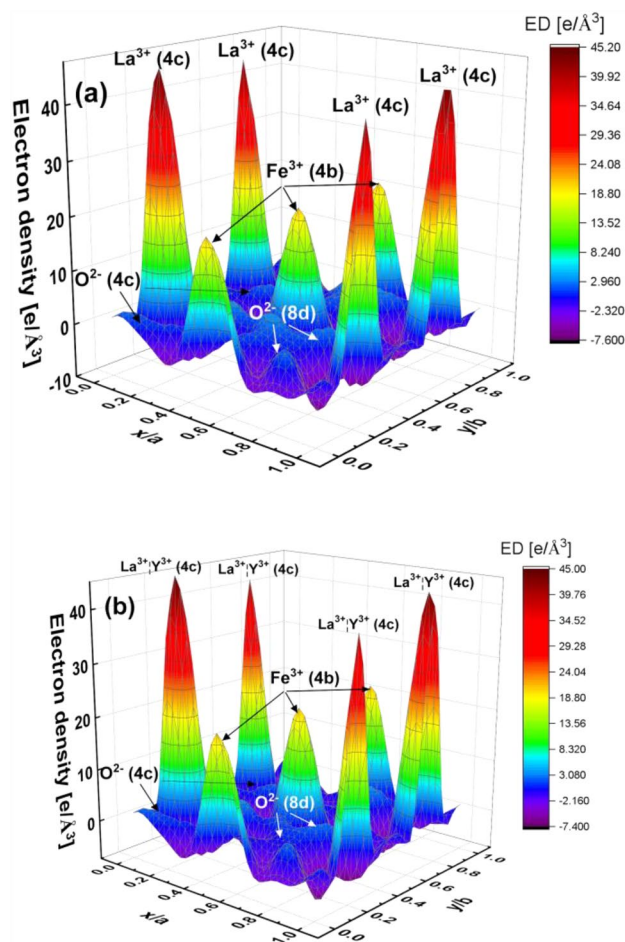


Fig. 6 The three-dimensional electron density representation of the different atoms in the unit cell of Perovskites **a** LFO and **b** LFOY25. The La^{3+} is clearly located on 4c Wyckoff positions, Fe^{3+} on (4b) sites and O^{2-} on both 4c and 8d positions. The electron density is quantified in $\text{e} \text{ \AA}^{-3}$.

observed to be an amalgamation of multiple semi-spherical primary particles that were slightly aggregated. The observed variations in particle size values, as determined by HRTEM and XRD analysis, can be attributed to the agglomeration of particles in the samples. The process of measuring the size of individual non-coalesced spherical particles is relatively uncomplicated. Nevertheless, determining precise size statistics for nanoparticles can be more intricate when they are aggregated or exhibit non-uniform shapes. Table 1 displays the estimated mean size of particles as determined from the TEM images. It is evident from Table 1 that the estimated particle size closely matches the one calculated from SSP through XRD analysis.

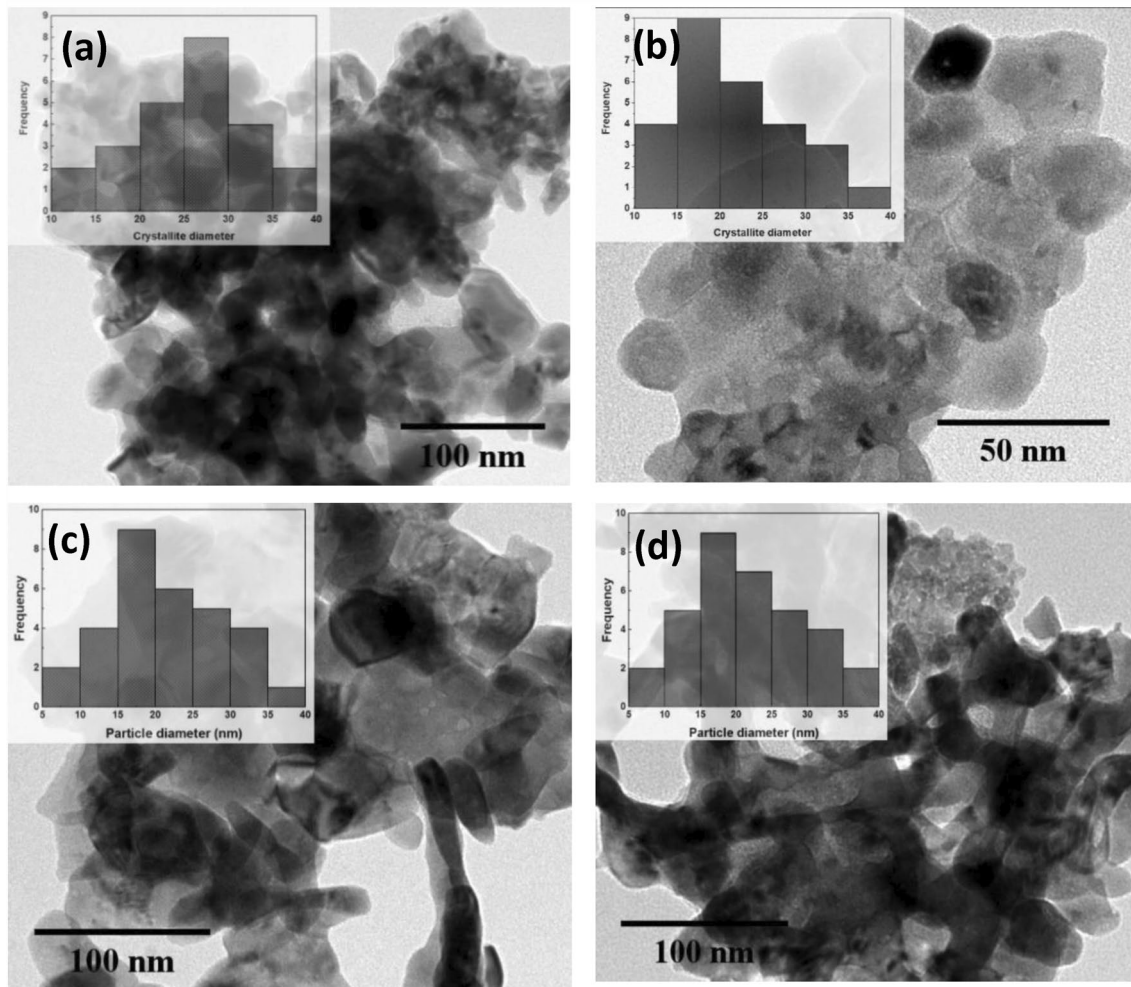


Fig. 7 HRTEM micrographs of the perovskites **a** LFO, **b** LFOY05, **c** LFOY15, and **d** LFOY30

Table 1 The estimated particle size for the typical fabricated orthoferrites

Composition	Sample code	Particle size (nm)
LaFeO ₃	LFO	25.00 ± 0.921
La _{0.95} Y _{0.05} FeO ₃	LFOY05	20.15 ± 0.950
La _{0.85} Y _{0.15} FeO ₃	LFOY15	20.68 ± 0.991
La _{0.70} Y _{0.30} FeO ₃	LFOY30	20.65 ± 1.010

3.3 Dielectric characterization and AC conductivity studies

3.3.1 Dependence of dielectric constant ($\epsilon_1(\omega)$, $\epsilon_2(\omega)$) on frequency

Investigating dielectric properties is an essential component furnishing crucial insights into

conduction mechanisms. This information can be utilized to comprehend the fundamental principles underlying dielectric losses, dipolar relaxation time, and activation energy [43]. The expression of dielectric permittivity is frequently represented as a complex quantity, as stated in reference [44].

$$\epsilon(\omega) = \epsilon_1(\omega) + \epsilon_2(\omega) \quad (5)$$

The real part denoted $\epsilon_1(\omega)$ corresponds to the relative permittivity or dielectric function, while the imaginary part $\epsilon_2(\omega)$ signifies the loss factor. Furthermore, the real component pertains to the capacitive characteristics of the substance, serving as a metric that characterizes the restorable energy accumulated in the material through polarization. On the other hand, the imaginary component represents a gauge of the energy necessary for molecular motion [45]. The

values of $\epsilon_1(\omega)$ and $\epsilon_2(\omega)$ were estimated based on the determined values obtained from the Hioki HiTester, utilizing the Eqs. (6 and 7) [43].

$$\epsilon_1(\omega) = Cd/\epsilon_0A, \tag{6}$$

$$\epsilon_2(\omega) = \epsilon_1(\omega) \tan \varphi, \tag{7}$$

where ϵ_0 is the permittivity of free space, and C is the capacitance and φ is the dielectric loss angle. The frequency dependences of the real dielectric constant have been investigated for the series of $\text{La}_{1-x}\text{Y}_x\text{FeO}_3$, ($x=0.0, 0.1, 0.15, 0.25,$ and 0.30) in the desired frequency as shown in Fig. 8. The aforementioned samples demonstrate a typical pattern of normal dispersion, wherein high dielectric constant values are observed at low frequencies. At lower frequencies, the real dielectric values exhibit a decreasing trend across all concentrations as frequency increases. However, at higher frequencies, these values approach a constant value as frequency increases. This phenomenon can be attributed to the fact that at lower frequencies, there is a contribution from multiple components of polarization, and the dipoles have the capacity to align themselves and contribute to the overall polarization. However, at higher frequencies, the dipoles cannot rotate at a sufficient speed in response to the changing field, leading to this behavior [46–49]. Furthermore, an increase in dopant concentration has been seen to improve dielectric constant values, while LFOY30

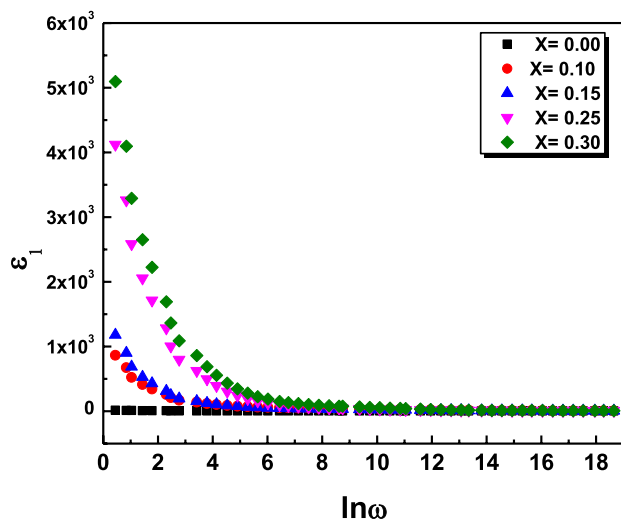


Fig. 8 The dielectric constant’s real part as a frequency function at different concentrations for $\text{La}_{1-x}\text{Y}_x\text{FeO}_3$, ($x=0.0, 0.10, 0.15, 0.25,$ and 0.30)

composition has a high dielectric constant due to stabilized and reinforced YFeO_3 . It has been concluded that Y^{3+} ions are successfully integrated into YFeO_3 as a result [26].

The imaginary part $\epsilon_2(\omega)$ can be evaluated as a function of frequency for the LFYO system, as depicted in Fig. 9. It has been noticed that $\epsilon_2(\omega)$ values reduce as the frequency increases at low frequencies. This phenomenon can be attributed to the essential source of the dielectric loss of the material, which is the migration of ions [50]. The perovskite series $\text{La}_{1-x}\text{Y}_x\text{FeO}_3$, where x takes values of 0.00, 0.1, 0.15, 0.25, and 0.30, exhibits constant values in $\epsilon_2(\omega)$ at high frequency. This phenomenon can be attributed to ion vibrations, which serve as the sole cause of dielectric loss [51]. On the other hand, the values $\epsilon_2(\omega)$ increase as Y concentration increases. The results indicate a significant impact of the concentration of Y cations in the perovskite system $\text{La}_{1-x}\text{Y}_x\text{FeO}_3$ on the values of the dielectric constant, as illustrated in Fig. 9.

3.3.2 Dependence of dielectric constant ($\epsilon_1(\omega), \epsilon_2(\omega)$) on temperature

The temperature dependence of the dielectric constant $\epsilon_1(\omega)$ at various frequencies for LFO and LFOY30 is shown in Fig. 10a, b. As the temperature rises over the entire frequency range, $\epsilon_1(\omega)$ increases. At low temperatures, the dipoles cannot align themselves with the direction of the applied field, resulting in a

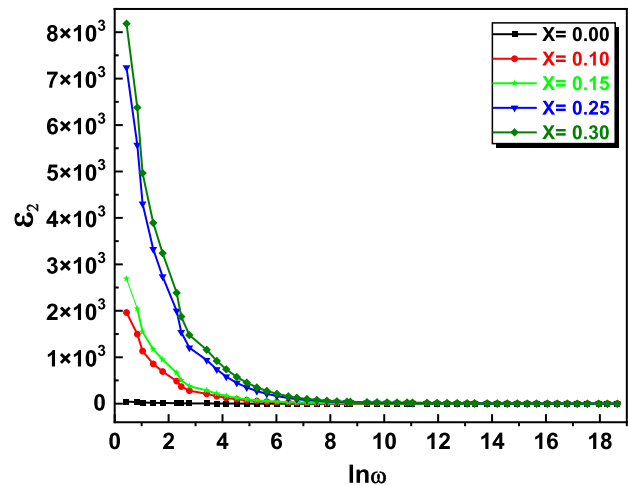


Fig. 9 The dielectric constant’s imaginary part as a frequency function at different concentrations for $\text{La}_{1-x}\text{Y}_x\text{FeO}_3$, ($x=0.0, 0.10, 0.15, 0.25,$ and 0.30)

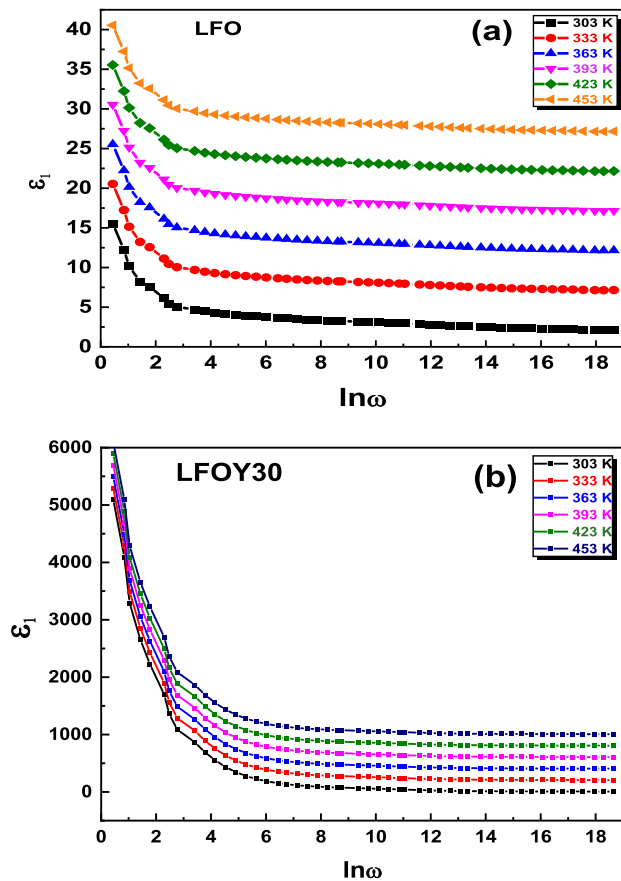


Fig. 10 The variation of the dielectric constant's real part with the frequency's logarithm at different temperatures for perovskites **a** LFO and **b** LFOY30

limited contribution to polarization. As temperature rises across the entire frequency range, there is a corresponding increase in polarization level. However, at lower temperatures, the dipoles seem incapable of orienting themselves in the direction of the applied field. This phenomenon leads to a restricted contribution to the overall polarization. The rise in temperature causes the orientation of dipoles to become more uniform, which leads to an increase in orientation polarization. This increase is reflected in the values of $\epsilon_1(\omega)$. At higher temperatures, the orientation of dipoles becomes more unrestricted, resulting in a decrease in the impact of molecular interaction energy relative to thermal energy. This leads to a rise in $\epsilon_1(\omega)$ values with an increase in temperature, as reported in previous studies [50, 52, 53].

Figure 11a, b illustrates the temperature dependence of $\epsilon_2(\omega)$ at different frequencies for perovskite compositions LFO and LFOY30. It is noticed that $\epsilon_2(\omega)$

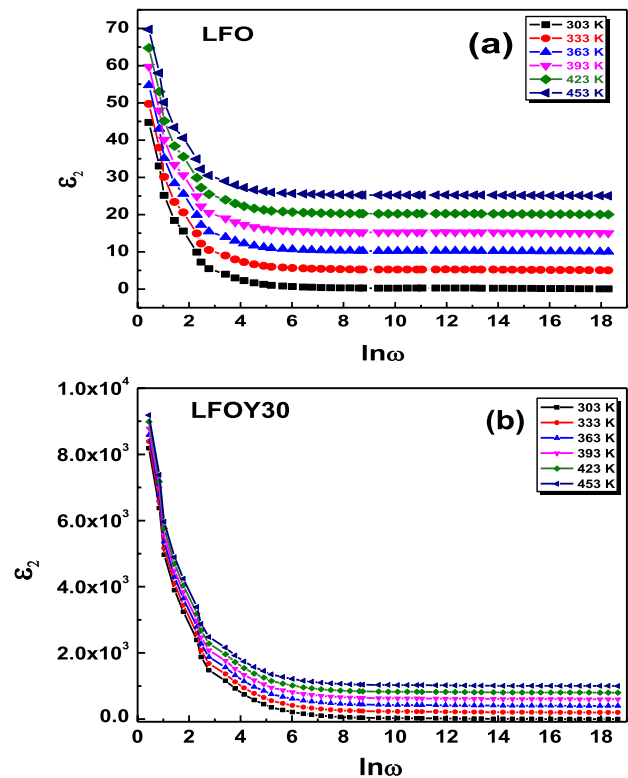


Fig. 11 The variation of the dielectric constant's imaginary part with the frequency's logarithm at different temperatures for perovskites **a** LFO and **b** LFOY30

values exhibit the same trend as $\epsilon_1(\omega)$ values. The values of $\epsilon_2(\omega)$ increase with increasing temperature in the ranges of studied temperature and frequency. At high temperatures, conduction, dipole, and vibrational losses play a vital role in the values of $\epsilon_2(\omega)$. On the other hand, dipole, conduction, and vibrational losses have the minimum values at low temperatures, reflecting the values of $\epsilon_2(\omega)$ [50].

3.3.3 Dependence of AC conductivity on frequency and temperature

The investigation of the transport phenomenon's conduction mechanism involves analyzing the frequency and temperature dependence of the AC conductivity. The determination of the AC conductivity relies on the values of the dielectric constant [51, 52]. The AC conductivity's frequency variation for the Perovskite system $\text{La}_{1-x}\text{Y}_x\text{FeO}_3$ ($x = 0.0, 0.10, 0.15, 0.25$ and 0.30) is illustrated in Fig. 12. The observed increase in conductivity values with increasing yttrium concentration can

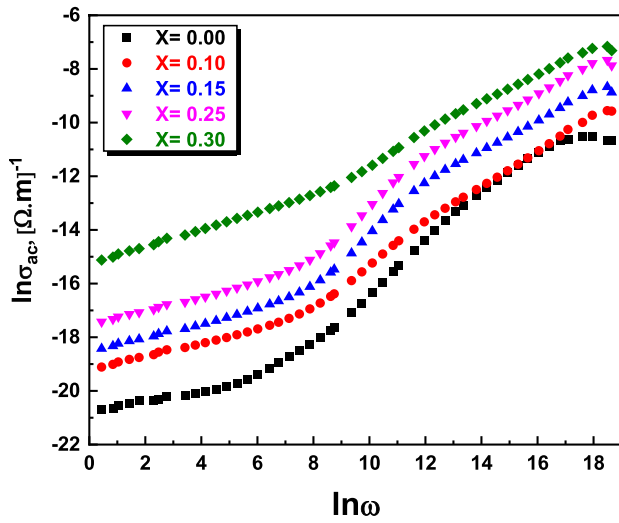


Fig. 12 The variation of AC conductivity with the frequency for the series of perovskite $\text{La}_{1-x}\text{Y}_x\text{FeO}_3$, ($x=0.00, 0.1, 0.15, 0.25,$ and 0.30)

be attributed to the presence of Fe^{4+} and Fe^{5+} ions that serve as electric charge carrier compensators [50]. The variation of the AC conductivity with the frequency for perovskites LFO and LFOY30 at various temperatures is illustrated in Fig. 13a, b. The AC conductivity rises with both frequency and temperature; this trend indicates that the perovskite system $\text{La}_{1-x}\text{Y}_x\text{FeO}_3$ behaves as a semiconductor material. Additionally, the conductivity increase with temperature indicates that the conduction process had been thermally activated. This increase can be attributed to increased charge carrier drift mobility after annealing [50]. The frequency dependence of AC conductivity is described by Jonsher’s power law [54].

$$\sigma_{AC} = A' \omega^s, \tag{8}$$

where A' represents a temperature-dependent constant and s is the frequency exponent, with a value in the range ($0 < s < 1$). It is worth mentioning that s is the slope of the straight lines at the high-frequency region of the graph in Fig. 13. The values of s decrease with increasing temperature, as shown in Fig. 14 for perovskites LFO and LFOY30. These behaviors have been explained by the correlated barrier hopping (CBH) model. This model suggests that charge transport is a thermally activated process. Additionally, the charge carrier hops between two defects over the potential barrier separating them, and then the potential barrier

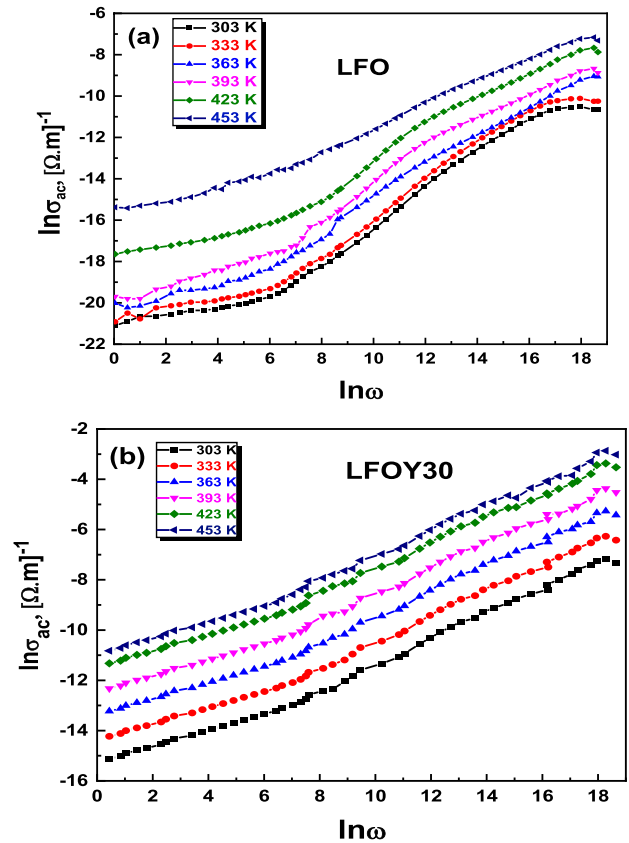


Fig. 13 The variation of the AC conductivity with frequency for perovskites **a** LFO and **b** LFOY30 at different temperatures

will be decreased by the Coulomb interaction [55]. The maximum value of barrier height, W_M , can be determined from s values as follows:

$$s = 1 - \frac{6k_B T}{W_M} \tag{9}$$

The slope of the relation between $(1 - s)$ and T has been used to determine the value of W_M , as illustrated in the inset of Fig. 14. The W_M value was determined to be approximately 0.26 eV.

The relation between temperature and AC conductivity can be expressed as [56]:

$$\sigma_{AC}(\omega) = \sigma_0 \exp\left(-\frac{\Delta E_{AC}}{k_B T}\right) \tag{10}$$

The values of AC activation energy (ΔE_{AC}) can be calculated from the slope of the relation between $\ln \sigma_{AC}$ and $\frac{1000}{T}$ at different frequencies for LFO and LFOY30, as seen in Fig. 15a, b. As presented in

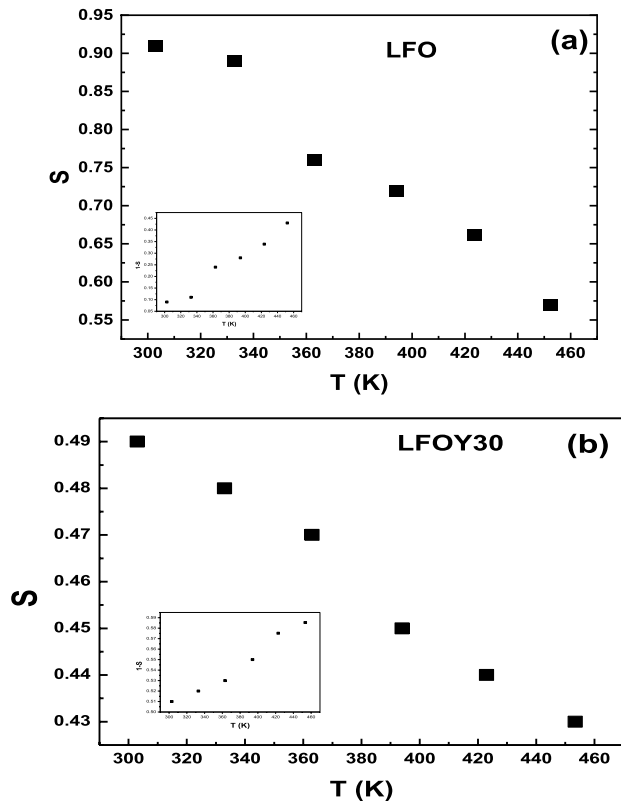


Fig. 14 The relation between the exponent factor and temperature for perovskites **a** LFO and **b** LFOY30

Table 2, the ΔE_{AC} values decreased with frequency from 0.35 to 0.20 eV for LFO and from 0.34 to 0.21 eV for LFOY30. The observed decrease in the measured values can potentially be attributed to the influence of frequency on the CBH model, which has been suggested as a suitable conduction mechanism for $\text{La}_{1-x}\text{Y}_x\text{FeO}_3$ [55]. As a result, it can be inferred that an increase in frequency is associated with a corresponding increase in electronic jump between localized states. This finding is strongly supported by earlier research on Perovskites [47, 48].

Table 3 presents a comparison between the performance of LFOY30 and other Perovskites to highlight the significance and originality of the current work. [57–60]. The findings of the study indicate that LFOY30 exhibits a dielectric constant that is comparatively greater than the values reported in other scholarly literature. The high dielectric constant values for LFOY30 are recommended for energy storage in capacitance applications of small sizes and other electrical components. The variation of the dielectric constant values of Perovskites compounds, as seen in Table 3, is influenced by several variables, including

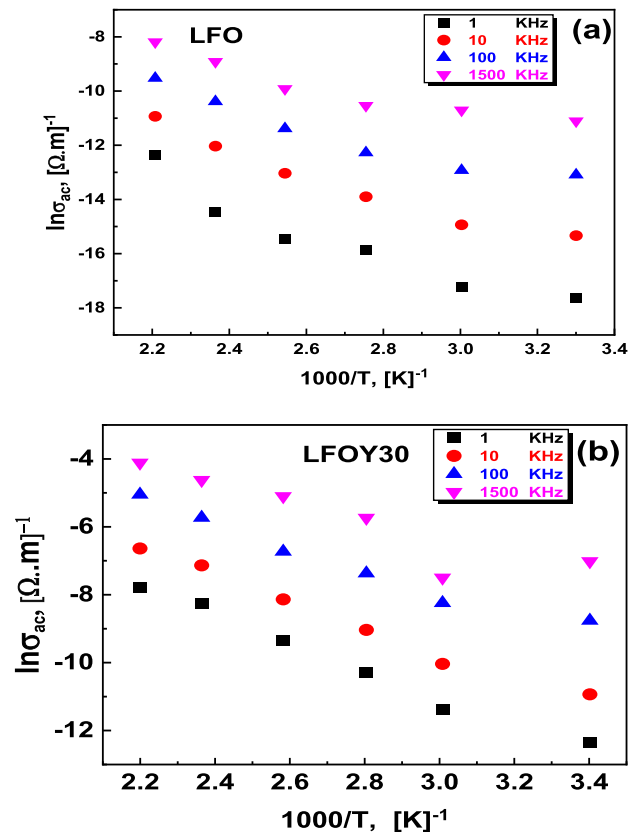


Fig. 15 The relation between $\ln \sigma_{AC}$ and $\frac{1000}{T}$ at different frequencies for perovskites **a** LFO and **b** LFOY30

temperature, mechanical stress, manufacture details, and voltage type.

3.3.4 Dependence of loss tangent on frequency and temperature

The degradation of electrical energy into the samples at various frequencies is measured by the loss tangent ($\tan \delta$). The loss tangent provides important details about the energy loss due to charge carrier conduction. The charge carriers' hopping induced the polarization.

Table 2 The estimated activation energy for LFO and LFOY30 at different frequencies

Frequency (KHz)	LFO ΔE_{ac} (eV)	LFOY30 ΔE_{ac} (eV)
1	0.35	0.34
10	0.33	0.32
100	0.27	0.26
150	0.20	0.21

Table 3 Comparison between the dielectric properties of the LFOY30 and other Perovskites

Perovskite	ϵ_1	ϵ_2	Temperature (K)	$\text{Ln}\sigma_{ac} (\Omega.m)^{-1}$	Conduction mechanism	References
$\text{La}_{0.70}\text{Y}_{0.30}\text{FeO}_3$ (LFOY30)	7 → 5890	0.3 → 9184	303 → 453	- 15 → - 3	CBH model	Current work
$\text{PrFe}_{0.5}\text{Cr}_{0.5}\text{O}_3$	1 → 1100	1.0 → 1000	298 → 423	- 23.8 → - 110	-	[57]
YbFeO_3	1 → 1000	-	313 → 573	-	-	[58]
LaBaFeTiO_6	210 → 550	-	298 → 573	- 10.5 → - 6	NSPT model CBH model	[59]
EuBaFeTiO_6	48 → 92	-	298 → 573	- 12 → - 8	NSPT model CBH model	[59]
BiFeO_3	0.01 → 1400	1.0 → 10000	400 → 475	-	-	[60]

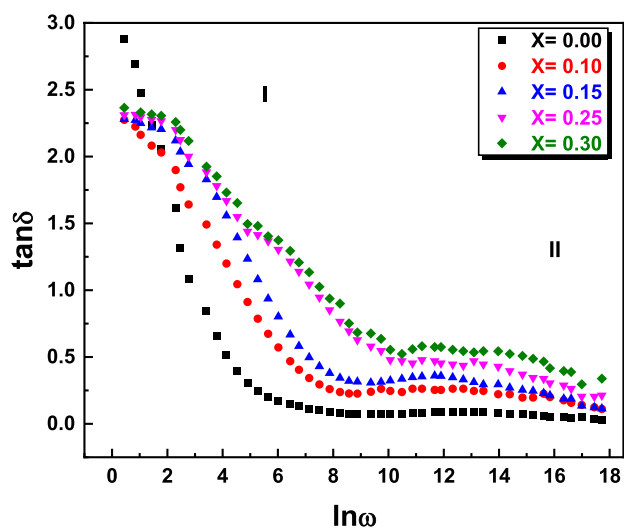


Fig. 16 The variations of loss tangent with angular frequency at various concentrations for the perovskite system $\text{La}_{1-x}\text{Y}_x\text{FeO}_3$

The dielectric loss happens when this polarization lags behind the AC electric field due to impurities and defects [61]. The loss tangent can be calculated by dividing the values of $\epsilon_2(\omega)$ by $\epsilon_1(\omega)$ [55].

The variations of loss tangent with angular frequency for the Perovskite system $\text{La}_{1-x}\text{Y}_x\text{FeO}_3$ ($x = 0.0, 0.1, 0.15, 0.25,$ and 0.30) are represented in Fig. 16. It can be asserted that in the initial region, the values of $\tan \delta$ experienced a rapid decrease, followed by a subsequent stabilization in the second region for all samples. The high values of $\tan \delta$ at low frequencies arise from multiple polarizations, which undeniably cause the loss to become high. Furthermore, the constant values of $\tan \delta$ in the second region are irrefutable evidence of the exclusive presence of electronic polarization [56]. On the other hand, the impact of temperature on the values of $\tan \delta$ for perovskite compositions LFO and LFOY30 is illustrated in Fig. 17a, b. The data suggest that

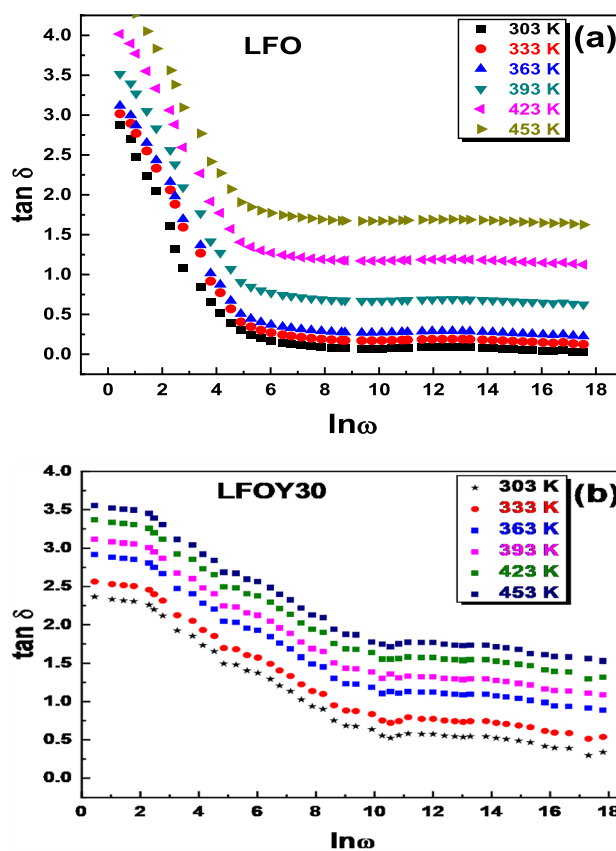


Fig. 17 The loss tangent as a function of angular frequency at different temperatures for perovskites **a** LFO and **b** LFOY30

the loss tangent’s behavior remains constant with temperature, while its values exhibit a noticeable increase at higher temperatures. This may be due to generating electrons and holes as the temperature rises [55]. On the other hand, the increasing of loss factor values with temperature is related to the rising of conduction electrons due to thermal activation at high temperatures. Also, the reduction in $\tan \delta$ values

represents fewer electrically active defects at higher frequencies [62].

4 Conclusion

The Sol-gel auto-combustion approach has been used to synthesize a series of $\text{La}_{1-x}\text{Y}_x\text{FeO}_3$ ($x = 0.00, 0.05, 0.10, 0.15, 0.25,$ and 0.30) orthoferrites. Through a comprehensive structural investigation utilizing XRD analysis, it has been ascertained that all compositions exhibiting orthorhombic structures with a space group Pnma are confirmed to exist as single phases without impurities. The tolerance factor calculations verified the composition stability of the prepared orthoferrites. Due to the difference in ionic radii between La^{+3} (1.16 \AA) and Y^{+3} (1.019 \AA) ions, the values of the tolerance factor descended as Y-content increased at La^{+3} tetrahedral sites. The size-strain plots based on the refined XRD data were utilized to estimate the mean crystallite size of the prepared samples and show variety from 11.9 to 18.5 nm. HRTEM micrographs are also used for further illustration of the microstructure of the prepared perovskites $\text{La}_{1-x}\text{Y}_x\text{FeO}_3$. The particles were discovered to be semi-spherical, and the estimated particle size is consistent with X-ray crystallite size. The electron density representation of the unit cell of $\text{La}_{1-x}\text{Y}_x\text{FeO}_3$ perovskites reveals an increase in density surrounding the lanthanum cation (A-site) as well as relatively substantial displacements in the different oxygen locations in the unit cell as compared to the Fe, Y, and La positions. The strong positive mountains correspond to the La^{3+} (4c) Wyckoff positions. In investigations on electrical conductivity, dielectric constant, and loss tangent behavior of $\text{La}_{1-x}\text{Y}_x\text{FeO}_3$ with varying dopant concentrations, results showed significant alters in the dielectric polarization and electrical conduction. It has been found that adding a dopant concentration greatly raises the dielectric constant, loss tangent, and conductivity over the full experimental frequency range of 50 Hz to 2 MHz, all of which have greater values than the undoped sample. The study underscores the importance of understanding the impact of dopant concentration on the properties of materials, which can aid in designing new materials with tailored properties for specific electronic applications. Additionally, the study investigated the effects of temperature and frequency on the AC conductivity and

dielectric characteristics of LFO and LFOY30 samples in the temperature range of 303 K to 453 K. Jonscher's power law was used to describe the AC conductivity, and the CBH model was identified as a suitable conduction mechanism. The activation energy values at 1 kHz were estimated to be 0.35 eV and 0.34 eV for LFO and LFOY30, respectively. The dielectric constant, loss tangent, and AC conductivity of both samples were found to be dependent on temperature and frequency. The results suggest that $\text{La}_{1-x}\text{Y}_x\text{FeO}_3$ samples are highly suitable for use in the production of microelectronic devices.

Acknowledgements

Not applicable.

Author contributions

Ahmed H. Ibrahim and S. Mosaad established the conceptualization of this study. They accomplished the investigation of this work, including the fabrication of the orthoferrite pellets and data collection, especially XRD and HRTEM. E. Elesh collected the electrical data for the study. Ahmed H. Ibrahim and S. Mosaad participated effectively in analyzing all the data related to the structure and microstructure of the prepared compositions, and E. Elesh analyzed the electrical data of the study. All the authors participated effectively in writing the Introduction, Materials and Methods, Characterization techniques, Abstract, and Conclusion sections. Furthermore, all authors discussed the results and commented on the paper, and they carried out a careful scientific and linguistic review of the research and checked the references as well.

Funding

Open access funding provided by The Science, Technology & Innovation Funding Authority (STDF) in cooperation with The Egyptian Knowledge Bank (EKB). No funding was obtained for this study.

Data availability

The data used to support the findings of this study are included in the article.

Declarations

Conflict of interest The author(s) declared no potential conflicts of interest with respect to the research, authorship, and publication of this article.

Supplementary Information The online version contains supplementary material available at <https://doi.org/10.1007/s10854-024-12110-9>.

Open Access This article is licensed under a Creative Commons Attribution 4.0 International License, which permits use, sharing, adaptation, distribution and reproduction in any medium or format, as long as you give appropriate credit to the original author(s) and the source, provide a link to the Creative Commons licence, and indicate if changes were made. The images or other third party material in this article are included in the article's Creative Commons licence, unless indicated otherwise in a credit line to the material. If material is not included in the article's Creative Commons licence and your intended use is not permitted by statutory regulation or exceeds the permitted use, you will need to obtain permission directly from the copyright holder. To view a copy of this licence, visit <http://creativecommons.org/licenses/by/4.0/>.

References

1. A. De, R. Ranjan, Large structural heterogeneity in sub-micrometer BaTiO₃ revealed via Eu⁺³ photoluminescence study. *J. Appl. Phys.* **128**, 1–11 (2020). <https://doi.org/10.1063/5.0011930>
2. G. Das Adhikary, R. Ranjan, Abrupt change in domain switching behavior within tetragonal phase regime of (x) Na_{1/2}Bi_{1/2}TiO₃-(1-x)K_{1/2}Bi_{1/2}TiO₃. *J. Appl. Phys.* **128**, 1–11 (2020). <https://doi.org/10.1063/5.0030195>
3. J. Yang, H. Zhong, M. Li, L. Zhang, Y. Zhang, Markedly enhancing the visible-light photocatalytic activity of LaFeO₃ by post-treatment in molten salt. *React. Kinet. Catal. Lett.* **97**, 269–274 (2009). <https://doi.org/10.1007/s11144-009-0025-1>
4. S. Chauhan, S.K. Jaiswal, Investigation on structure and stability of cerium doped (Ba_{0.5}Sr_{0.5})(Fe_{1-x}Ce_x)O_{3-δ} (x = 0–1.0) oxides by Rietveld refinement. *Solid State Commun.* **334**, 114343 (2021)
5. S.K. Jaiswal, R. Ranjan, J. Kumar, Structural Mössbauer studies and oxygen permeation characteristics of Sr_{1-x}Ba_xFe_{1-y}Li_yO_{3-ξ} (x = 0, 0.5; y = 0–0.10) system. *J. Alloys Compds.* **844**(2020), 155832 (2020). <https://doi.org/10.1016/j.jallcom.2020.155832>
6. S.K. Jaiswal, K.J. Yoon, J.W. Son, J.H. Lee, Synthesis and investigation on stability and electrical conductivity of Ti-doped Ba₃CaTa_{2-x}Ti_xO₉ (0 ≤ x ≤ 1.0) complex oxides. *J. Alloys Compds.* **775**, 736–741 (2019). <https://doi.org/10.1016/j.jallcom.2018.10.185>
7. S.K. Jaiswal, Investigation on phase and Raman spectra of Ba₃(CaTa_{2-y}Ti_y)O_{9-δ} (y = 0–0.50) system. *J. Asian Ceram. Soc.* **3**, 572–577 (2020)
8. A. Fossdal, M.-A. Einarsrud, T. Grande, Mechanical properties of LaFeO₃ ceramics. *J. Eur. Ceram. Soc.* **25**(6), 927–933 (2005). <https://doi.org/10.1016/j.jeurceramsoc.2004.04.009>
9. W. Harona, A. Wisitorsaatb, S. Wongnawa, Nanostructured perovskite oxides – LaMO₃ (M = Al Co, Fe) prepared by co-precipitation method and their ethanol sensing characteristics. *Ceram. Int.* **43**, 5032–5040 (2017)
10. B.C. Steele, A. Heinzl, Materials for fuel-cell technologies. *Nature* **414**, 345–352 (2001). <https://doi.org/10.1038/35104620>
11. B. Deka, S. Ravi, A. Perumal, D. Pamu, Effect of Mn doping on magnetic and dielectric properties of YFeO₃. *Ceram. Int.* **43**, 1323e1334 (2017)
12. X. Zhang, H. Li, Y. Li, W. Shen, Structural properties and catalytic activity of Sr-substituted LaFeO₃ perovskite. *Chin. J. Catal.* **33**, 1109–1114 (2012)
13. X.N. Ying, Charge order suppression in oxygen nonstoichiometric La_{1/3}Sr_{2/3}FeO_{3-δ}. *Solid State Commun.* **169**, 20–23 (2013)
14. K. Mukhopadhyay, A.S. Mahapatra, P.K. Chakrabarti, Multiferroic behavior, enhanced magnetization and exchange bias effect of Zn substituted nanocrystalline LaFeO₃ (La(1-x)Zn_xFeO₃, x = 0.10 and 0.30). *J. Magn. Magn. Mater.* **329**, 133–141 (2013)
15. S. Acharya, P.K. Chakrabarti, Some interesting observations on the magnetic and electric properties of Al³⁺ doped lanthanum orthoferrite (La_{0.5}Al_{0.5}FeO₃). *Solid State Commun.* **150**, 1234–1237 (2010)
16. R. Andoulsin, K. Horchani-Naifer, M. Ferid, Electrical conductivity of La_{1-x}Ca_xFeO_{3-δ} solid solutions. *Ceram. Int.* **39**, 6527–6531 (2013)
17. C. Xiangfeng, P. Siciliano, CH₃SH-sensing characteristics of LaFeO₃ thick-film prepared by co-precipitation method. *Sens. Actuators, B: Chem.* **94**, 197–200 (2003)
18. X.-P. Xiang, L.-H. Zhao, B.-T. Teng, J.-J. Lang, X. Hu, T. Li, Y.-A. Fang, M.-F. Luo, J.-J. Lin, Catalytic combustion

- of methane on $\text{La}_{1-x}\text{Ce}_x\text{FeO}_3$ oxides. *Appl. Surf. Sci.* **276**, 328–332 (2013)
19. S. Thirumalairajan, K. Girija, I. Ganesh, D. Mangalaraj, C. Viswanathan, A. Balamurugan, N. Ponpandian, Controlled synthesis of perovskite LaFeO_3 microsphere composed of nanoparticles via self-assembly process and their associated photocatalytic activity. *Chem. Eng. J.* **209**, 420–428 (2012)
 20. J. Leng, S. Li, Z. Wang, Y. Xue, D. Xu, Synthesis of ultrafine lanthanum ferrite (LaFeO_3) fibers via electrospinning. *Mater. Lett.* **64**, 1912–1914 (2010)
 21. G. Pecchi, P. Reyes, R. Zamora, C. Campos, L.E. Cadús, B.P. Barbero, Effect of the preparation method on the catalytic activity of $\text{La}_{1-x}\text{Ca}_x\text{FeO}_3$ perovskite-type oxides. *Catal. Today* **133–135**, 420–427 (2008)
 22. S.R. Wadgane, S.E. Shirsath, A.S. Gaikwad, S. Satpute, A. Kadam, R. Kadam, Ferro and magneto-electric characteristics in $\text{YFeO}_3\text{–Y}_3\text{Fe}_5\text{O}_{12}$ nanocomposites. *J. Magn. Magn. Mater.* **457**, 103–109 (2018)
 23. D. Triyono, C.A. Kafa, H. Laysandr, Effect of Sr-substitution on the structural and dielectric properties of LaFeO_3 perovskite materials. *J. Adv. Dielectr.* **8**(5), 1850036 (2018). <https://doi.org/10.1142/S2010135X18500364>
 24. L. John Berchmans, R. Sindhu, S. Angappan, C.O. Augustin, Effect of antimony substitution on structural and electrical properties of LaFeO_3 . *J. Mater. Process. Technol.* **207**(1–3), 301–306 (2008). <https://doi.org/10.1016/j.jmatp rotec.2008.06.054>
 25. A. Tiwari, P. Jain, O. Subohi, Dielectric and electrical properties of barium and nickel doped LaFeO_3 . *ECS J. Solid State Sci. Technol.* **10**, 103009 (2021). <https://doi.org/10.1149/2162-8777/ac2b3f>
 26. M. Asif, M. Azhar Khan, S. Atiq, T. Alshahrani, Q. Mahmood, N.A. Kattan, A. Manzoor, *Ceram. Int.* **47**(5), 6663–6674 (2021). <https://doi.org/10.1016/j.ceramint.2020.11.005>
 27. J.T. Chambi, L.D. Prado, B.F. de Carvalho Patricio, M. Ceballos, I. Bianco, C. Fandaruff, H.V. Antunes Rocha, A. Kuznetsov, S.L. Cuffini, Quantitative analysis and evaluation of solid-state stability of mebendazole forms A and C suspensions by powder X-ray diffraction using the Rietveld method. *Int. J. Pharm.* **650**, 123721 (2024). <https://doi.org/10.1016/j.ijpharm.2023.123721>
 28. K.R. Desai, S.T. Alone, S.R. Wadgane, S.E. Shirsath, K.M. Batoo, A. Imran, E.H. Raslan, M. Hadi, M.F. Ijaz, R.H. Kadam, X-ray diffraction based Williamson-Hall analysis and rietveld refinement for strain mechanism in Mg–Mn co-substituted CdFe_2O_4 nanoparticles. *Phys. B: Condens.* **614**, 413054 (2021). <https://doi.org/10.1016/j.physb.2021.413054>
 29. A.M. Nawar, S. Mosaad, A.H. Ibrahim, Optical and structural characterizations of NiO-doped PMMA films and fabrication of Ag/NiO-doped PMMA/n-Si/AuSb for analogue-digital switching applications. *Phys. B: Condens.* **676**, 415624 (2024). <https://doi.org/10.1016/j.physb.2023.415624>
 30. M. Marezio, P.D. Dernier, *Mater. Res. Bull.* **6**, 23–30 (1971)
 31. H.M. Rietveld, *Acta Crystallogr.* **22**, 151 (1967)
 32. H.M. Rietveld, *J. Appl. Crystallogr.* **2**, 65 (1969)
 33. H. Es-soufi, H. Bih, L. Bih, R. Rajesh, A.R.F. Lima, M.I. Sayyed, R. Mezher, Rietveld refinement, structural characterization, and methylene blue adsorption of the new compound $\text{Ba}_{0.54}\text{Na}_{0.46}\text{Nb}_{1.29}\text{W}_{0.37}\text{O}_5$. *Crystals* **12**, 1695 (2022). <https://doi.org/10.3390/cryst12121695>
 34. S. Vibha, A. Sanghi, M. Agarwal, E. Chauhan, A. Arya, S. Kumari, P. Kaushik, P. Sharma, Crystal structure determination, XRD peak profile analysis and morphological study of double perovskite SrNdFeTiO_6 . *Mater. Today: Proc.* **82**, 79–84 (2023). <https://doi.org/10.1016/j.matpr.2022.11.364>
 35. S. Bid, S.K. Pradhan, *Mater. Chem. Phys.* **82**, 27 (2003)
 36. J. Córdova-Calderón, P.V. Tuza, M.M.V.M. Souza, Synthesis and characterization of $\text{LaNi}_{0.5}\text{Ti}_{0.5}\text{O}_3$ and $\text{La}_2\text{NiTiO}_6$ double perovskite nanoparticles. *Materials (Basel)* **15**(7), 2411 (2022). <https://doi.org/10.3390/ma15072411>
 37. Y. Sakai, D. Urushihara, T. Asaka, K. Fukuda, Z. Yang, N. Tanibata, H. Takeda, M. Nakayama, Octahedral tilting and modulation structure in perovskite-related compound $\text{La}_{1/3}\text{NbO}_3$. *Phys. Status Solidi* **259**, 2100561 (2022). <https://doi.org/10.1002/pssb.202100561>
 38. A.H. Ibrahim, Y.M. Abbas, H.A. Ayoub, M.H. Ali, M. Aldoori, Novel synthesis of stabilized $\text{Bi}_{1-x-y}\text{Gd}_x\text{Dy}_y\text{O}_{1.5}$ solid electrolytes with enhanced conductivity for intermediate temperature solid oxide fuel cells (SOFCs). *J. Rare Earths* (2023). <https://doi.org/10.1016/j.jre.2023.10.003>
 39. A.H. Ibrahim, Y.M. Abbas, R.A. Abdel, S.M. Aziz, The influence of spin state of the Cr ions on the structural and magnetic behavior of orthorhombic $\text{LaFe}_{1-x}\text{Cr}_x\text{O}_3$ perovskites ($0.0 < x < 0.5$). *J. Mater. Sci. Mater. Electron.* **34**, 830 (2023). <https://doi.org/10.1007/s10854-023-10200-8>
 40. Y.M. Abbas, A.B. Mansour, S.E. Ali, A.H. Ibrahim, Investigation of structural and magnetic properties of multiferroic $\text{La}_{1-x}\text{Y}_x\text{FeO}_3$ perovskites, prepared by citrate auto-combustion technique. *J. Magn. Magn. Mater.* **482**, 66–74 (2019). <https://doi.org/10.1016/j.jmmm.2019.03.056>
 41. R.L. Cook, A.F. Sammells, On the systematic selection of perovskite solid electrolytes for intermediate temperature

- fuel cells. *Solid State Ionics* **45**, 311–321 (1991). [https://doi.org/10.1016/0167-2738\(91\)90167-A](https://doi.org/10.1016/0167-2738(91)90167-A)
42. H. Bantikatla, L.N.S.M.P. Devi, R.K. Bhogoju, Microstructural parameters from X-ray peak profile analysis by Williamson-Hall models; A review. *Mater. Today: Proc.* **47**, 4891–4896 (2021). <https://doi.org/10.1016/j.matpr.2021.06.256>
43. R.L. Cook, A.F. Sammells, *Solid State Ion.* **45**, 311–321 (1991)
44. A. Saif, P. Poopalan, *J. Mater. Sci. Technol.* **27**, 802 (2011)
45. T. Sankarappa, M. Prashant Kumar, G.B. Devidas, N. Nagaraja, R. Ramakrishnareddy, *J. Mol. Struct.* **88**, 308 (2008). <https://doi.org/10.1016/j.molstruc.2008.02.009>
46. M. Abd-el Salam, H.M. El-Mallah, D.G. El-Damhogi, E. Elesh, *J. Electron. Mater.* **50**, 562–570 (2020)
47. H.M. El-Mallah, *Acta Phys. Pol., A* **122**, 174 (2012)
48. A. Jamil, I. Rashid, W. Khan, S. Bajwa, A. Rehman, M.A. Rafiq, *Physica E* **154**, 115794 (2023). <https://doi.org/10.1016/j.physe.2023.115794>
49. M. El-Nahass, E. Mossad, A. Farag, S. Menshawy, F. Abu-Samaha, E. Elesh, *IOSR J. Appl. Phys* **6**, 22–29 (2014)
50. K. Mahato, A. LoDutta, T. Sinha, Dielectric relaxation and ac conductivity of double perovskite oxide $\text{Ho}_2\text{ZnZrO}_6$. *Phys. B: Condens.* **406**, 2703–2708 (2011). <https://doi.org/10.1016/j.physb.2011.04.012>
51. T.M. Grant, N.A. Rice, L. Muccioli, F. Castet, B.H. Lassar, A.C.S. Appl. Electron. Mater. **1**, 494–504 (2019). <https://doi.org/10.1021/acsaelm.8b00113>
52. S. Mosaad, A.H. Ibrahim, E. Elesh, D.G. El-Damhogi, E. Elgazzar, Synthesis of prussian blue analog (Co/TCNi/HCCr) nanoparticles using a facile co-precipitation approach and evaluation of their dielectric characteristics for electronic applications. *J. Mater. Sci. Mater. Electron.* (2023). <https://doi.org/10.1007/s10854-023-11606-0>
53. E. Elesh, Z. Mohamed, M. Dawood, Temperature dependence of structure, morphology and dielectric characterization of gallium phthalocyanine chloride discs. *J. Electron. Mater.* **49**, 2633–2641 (2020). <https://doi.org/10.1007/s11664-020-07971-9>
54. A.M. Abdelghany, H.M. Zeyada, H.A. ElBatal, R.E. Fetouh, *SILICON* **9**, 347–354 (2017). <https://doi.org/10.1007/s12633-016-9498-5>
55. M.R. Anantharaman, S. Sindhu, S. Jagatheesan, K.A. Molini, P. Kurian, *J. Phys. D Appl. Phys.* (1999). <https://doi.org/10.1088/0022-3727/32/15/307>
56. J. Stevels, "Handbuch Der Physik, in *Flugge*". (Springer, Berlin, 1975), p.350
57. L. Boudad, M. Taibi, W. Belayachi, M. Abd-Lefdil, Investigation of magnetic, dielectric, optical, and electrical of Fe half-doped PrCrO_3 perovskite. *J. Solid-State Chem.* **309**, 122933 (2022). <https://doi.org/10.1016/j.jssc.2022.122933>
58. P. Sathish Kumar, M. Phebe Kokila, A.K. Kanagaraj, L.H. Paidi, H.A. Therese, S. Madeswaran, Solution combustion synthesis of rare earth orthoferrite nanoparticles: a comparative study on multiferroic properties of Er– FeO_3 vs (La, Yb) FeO_3 . *J. Superconductivity Novel Magn.* **33**, 3621–3629 (2020)
59. L. Boudad, M. Taibi, A. Belayachi, M. Abd-Lefdil, Structural, morphological, dielectric and optical properties of double perovskites RBaFeTiO_6 (R= La, Eu). *RSV Adv.* **11**, 40205 (2021)
60. S. Ahmed, S.K. Barik, S.K. Barik, A comparative study on structure and electrical properties of antimony ferrite and bismuth ferrite. *Appl. Phys. A* **124**, 523 (2018). <https://doi.org/10.1007/s00339-018-1900-2>
61. S.A. Fatima, R. Shaheen, K. Shahzad, Study of electrical and dielectric properties of $\text{Sr}_3\text{CoSb}_2\text{O}_9$ perovskite by impedance spectroscopy. *Appl. Phys. A* **127**, 466 (2021). <https://doi.org/10.1007/s00339-021-04597-4>
62. A. Jamil, I. Rashid, W.S. Khan, S.Z. Bajwa, A. Rehman, M.A. Rafiq, Leakage current, electrical properties and density of states extracted using correlated barrier hopping in perovskite layered aurivillius $\text{Bi}_5\text{Ti}_3\text{FeO}_{15}$ nanoparticles. *Phys. E: Low-Dimens. Syst. Nanostructures* **154**, 1157 (2023). <https://doi.org/10.1016/j.physe.2023.115794>

Publisher's Note Springer Nature remains neutral with regard to jurisdictional claims in published maps and institutional affiliations.